Article

Early-winter mixing event associated with baroclinic motions in weakly stratified Lake Biwa

Hikaru Homma,[1] Takeyoshi Nagai,[1] Kenji Shimizu,[2,3] and Hidekatsu Yamazaki[1]*

[1] *Tokyo University of Marine Science and Technology, Minato-ku, Tokyo, Japan*
[2] *Commonwealth Scientific and Industrial Research Organisation, Floreat, Western Australia, Australia*
[3] *Kitami Institute of Technology, Kitami-shi, Hokkaido, Japan.*
* *Corresponding author: hide@kaiyodai.ac.jp*

Received 8 June 2015; accepted 18 May 2016; published 13 July 2016

Abstract

The annual overturn of lake water (termed holomixis) during winter is essential in maintaining the environment of warm monomictic lakes by transporting heat and organic and inorganic constituents; however, direct observation of wintertime mixing processes is limited. To better understand the detailed physical processes responsible for holomixis, this study investigated a cold low-oxygen water intrusion event on the northeastern slope of weakly stratified Lake Biwa (Japan), observed using mooring systems. The intrusion occurred concurrently with superinertial oscillations of near-bottom currents. The effective Wedderburn number suggests that basin-scale Kelvin waves were excited by north-eastward winds (~4 m s^{-1}) prior to the intrusion event. The results of a modal analysis suggest that the intrusion was caused by a combination of Kelvin and Poincaré waves that locally uplifted the cold deep water. The heat budget analyses revealed that a substantial part of the intruded cold water was mixed diapycnally, induced by wind stirring, nighttime convection, and bottom friction. The superinertial currents enhanced the dissipation due to bottom friction by ~30%. The cold water intrusion and subsequent mixing provided local heat flux of 98 W m^{-2} over 6 days, which was 1.4 times larger than the average surface heat flux over the same period. In addition to previously studied processes, such as surface cooling and gravity currents from the shore, this study indicates that wind-induced baroclinic motions and subsequent diapycnal mixing of a stratified water column contribute to holomixis.

Key words: heat flux, holomixis, internal wave, Lake Biwa, mixing, Wedderburn number, wintertime cooling

Introduction

The annual overturn in warm monomictic lakes, classically termed holomixis (e.g., Melack and Jellison 1998), significantly affects the lake environment by transporting heat and organic and inorganic constituents. In particular, oxygen supply into deep water during holomixis is essential for maintaining lake environments and ecosystems (e.g., Yoshimizu et al. 2010). In recent years, it has become imperative to investigate the detailed physical processes of holomixis because climate change possibly leads to insufficient mixing during winter and oxygen depletion in warm monomictic lakes (e.g., Kumagai et al. 2003).

The primary driver of holomixis is convective mixing in winter (e.g., Marshall and Schott 1999, Nagai et al. 2005), but recent studies showed the importance of other 3-dimensional physical processes. An important process is gravity currents (Peeters and Kipfer 2009). In Lake Geneva, Fer et al. (2001) investigated gravity currents of cold water descending down the basin slope, which originated from the heat-capacity difference between a shallow shelf and the deeper lake interior. The numerical study by Akitomo et al. (2009a, 2009b) also suggested that the holomixis in Lake Biwa is associated with gravity currents descending the slopes. Another potential contributor is mixing due to basin-scale internal waves.

DOI: 10.5268/IW-6.3.898

For example, Rueda et al. (2003) reported that basin-scale internal waves were energized by storms during a weakly stratified season in Lake Tahoe; however, they did not investigate the effect of these waves on mixing. Unlike convective mixing and gravity currents, mixing due to basin-scale internal waves does not transport heat upward; however, it can contribute to holomixis by reducing the energy required to homogenize the lake through deepening of the thermocline and/or weakening of the stratification. Despite these studies, detailed physical processes contributing to holomixis and their relative importance are still not well understood, largely because direct observations of mixing events during winter are lacking.

To better understand the contributions from baroclinic motions to mixing in a weakly stratified lake, we investigated a cold water intrusion event on the northeastern slope of Lake Biwa in early winter observed using mooring systems. We introduce the study site, field data, and analysis methods and then describe the observed cold water intrusion event and discuss the effect of wind forcing on the basin-scale motions, properties of the internal waves, heat budget, and cause of the diapycnal mixing associated with the baroclinic motions, which have not been reported for wintertime lake mixing.

Materials and methods

Study site

Lake Biwa is the largest lake in Japan, located in central Honshu Island (Fig. 1a). Lake Biwa is 63 km long in the north–south direction and 23 km wide (Kawanabe et al. 2012) and consists of 2 basins: the shallower small South Basin and the deeper large North Basin. The maximum depth of the entire lake is 104 m at the northern part of the North Basin, and the average depths of the North Basin and South Basin are 44 and 3.5 m, respectively. The North Basin has gentle slopes in the south and east and steep slopes in the north and west.

Field data

Moorings

The mooring systems were deployed at mooring site Y, located in the middle of the northeastern slope in the North Basin of Lake Biwa (Fig. 1a). Wintertime advective processes have been reported around this site through both cross-sectional field surveys (Yoshimizu et al. 2010) and numerical simulations (Akitomo et al. 2009a, 2009b). Site Y

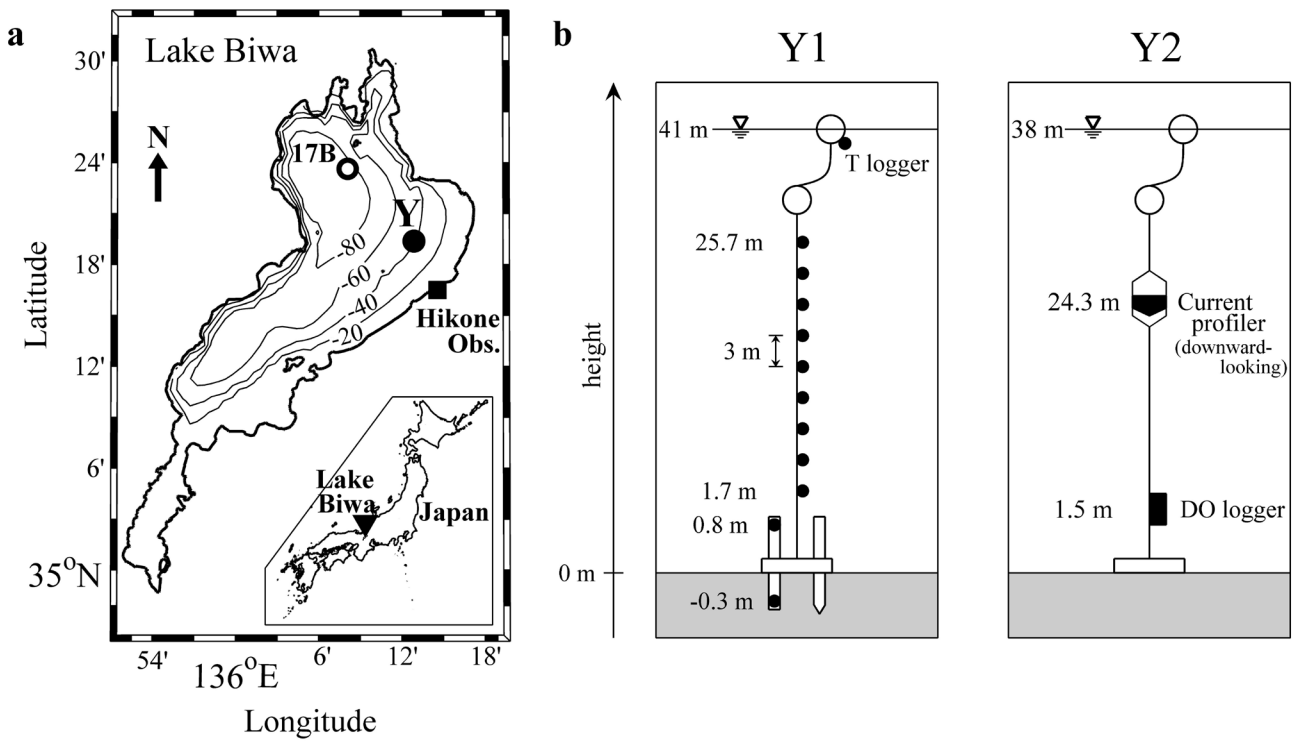

Fig. 1. Study site and mooring systems. (a) Bathymetric map of Lake Biwa and locations of mooring site Y (filled circle), Hikone Local Meteorological Observatory (filled square), and station 17B (open circle) of Shiga Prefecture (SPLBED 2010). Depth is indicated in negative values. Bottom right inset shows location of Lake Biwa on Honshu Island, Japan. (b) Composition of mooring systems Y1 and Y2 deployed at site Y. Levels of loggers are indicated in height from local lake bottom. Bottom part of Y1 was a pile anchor with temperature loggers to measure temperature of bottom water and sediment.

Table 1. Details of instrument deployment at site Y. TC = thermistor chain; T = temperature logger; DO = dissolved oxygen logger. Height range indicates levels of observed layers in height from local lake bottom.

Mooring	Latitude	Longitude	Depth (m)	Instrument	Height range (m)
Y1	35°19′27″N	136°12′39″E	41	Surface T	41 (surface)
				TC	1.7–25.7 (3 m interval)
				Bottom T	−0.3, 0.8
Y2	35°19′40″N	136°12′53″E	38	AWAC	1.9–23.9 (1 m interval)
				DO	1.5

was ~5 km from the closest shore, and the local depth was ~40 m. We deployed the mooring systems on 11 December 2009 (Julian day [JD] 345) and retrieved them on 18 March 2010 (JD 77). The Research Vessel (R/V) Hakken-go (Lake Biwa Environmental Research Institute, hereafter LBERI) provided a platform for the survey. We focused on the 10 d period from JD 352 to 362, late December when the cold water intrusion event was observed.

We deployed 2 mooring systems, Y1 and Y2, to measure the thermal stratification, dissolved oxygen (DO) concentration near the bottom, and velocity field (Fig. 1b and Table 1). The Y2 system was located ~540 m northeast of Y1 to prevent the 2 mooring systems from colliding.

The Y1 system consisted of a thermistor chain and bottom pile anchor (Fig. 1b). The thermistor chain (U22-001 and UTBI-001, Onset Computer Corporation) was mounted between 1.7 and 25.7 m above the bottom (Table 1). To measure sediment temperature as well as bottom water temperature, we also installed 2 temperature loggers (U22-001, UTBI-001) at the bottom part of the system, at both ends of a vertical pipe that penetrated the anchor (Fig. 1b and Table 1). An additional temperature logger (UTBI-001) was attached to a surface buoy to measure surface water temperature. The temperature loggers have a resolution of 0.02 °C, an accuracy of 0.2 °C, and response time (90%) of 5 min.

The Y2 system was equipped with a 1 MHz acoustic wave and current profiler (AWAC, Nortec AS) and a DO logger (ADOW-CMP, JFE Advantech Co., Ltd.). The downward-looking AWAC was mounted at the middle of the system (Fig. 1b) and measured velocity between 1.9 and 23.9 m above the bottom with a resolution of 1 m (Table 1). The accuracy of the AWAC velocity measurements is 1% of the measured value or 0.5 cm s^{-1}. The DO logger was installed 1.5 m above the bottom (Fig. 1b and Table 1). The oxygen sensor has an accuracy of 1% of the measured value.

All the instruments recorded data every 10 min. The AWAC recorded an ensemble average of 6 pings over 2 min at intervals of 10 min. The pitch and roll of the AWAC ranged from −1.1 to −0.3° and from −0.1 to 2.1°, respectively. The depth of the AWAC drifted <0.2 m during the observed period (JD 352–362), suggesting that the mooring was sufficiently taut. In this study, all collected time-series data were running-mean averaged over 1 h intervals unless otherwise stated.

Offshore station and weather station

To gain an idea of stratification at a deep point, we used temperature profiles obtained from the center of the lake basin (station 17B; Fig. 1a), observed twice a month by the environment department of Shiga Prefecture (SPLBED 2010).

In addition to the hydrographic and current data, we used meteorological data (JMA 2002) collected at a coastal weather station (Hikone Local Meteorological Observatory, Fig. 1a), the nearest (6 km) national weather station from the mooring site.

Analysis methods

Wind forcing

The Wedderburn number (Monismith 1985) is a useful index to evaluate the effects of wind forcing on stratified lakes. Assuming 2-layer stratification and a 2-dimensional basin shape, the effective Wedderburn number W_e (Shintani et al. 2010) extends the Wedderburn number to take the effects of linear bottom slopes into account and is defined as:

$$W_e = \frac{g' h_{1B}^2}{u_{s*}^2 L_e}, \quad (1)$$

where u_{s*} is the surface friction velocity in the water by wind stress, g' is the reduced gravity, h_{1B} is the distance from the surface to the depth corresponding to the middle of the tilted interface between the surface and bottom layers, and L_e is the horizontal length of the tilted interface. The surface friction velocity is estimated from $u_{s*} = (\rho_a C_{Ds} U_{10}^2/\rho_w)^{1/2}$, where ρ_a = 1.2 kg m^{-3} is the air density, ρ_w = 1000 kg m^{-3} is the water density, U_{10} is the wind speed 10 m above the water surface, and C_{Ds} is the surface drag coefficient (~0.0013; e.g., Boegman 2009). The variables h_{1B}, L_e, and W_e are estimated through the iteration procedure (Shintani et al. 2010) to determine tilting of the interface, which depends on the balance between the wind disturbance force and the baroclinic

 DOI: 10.5268/IW-6.3.898

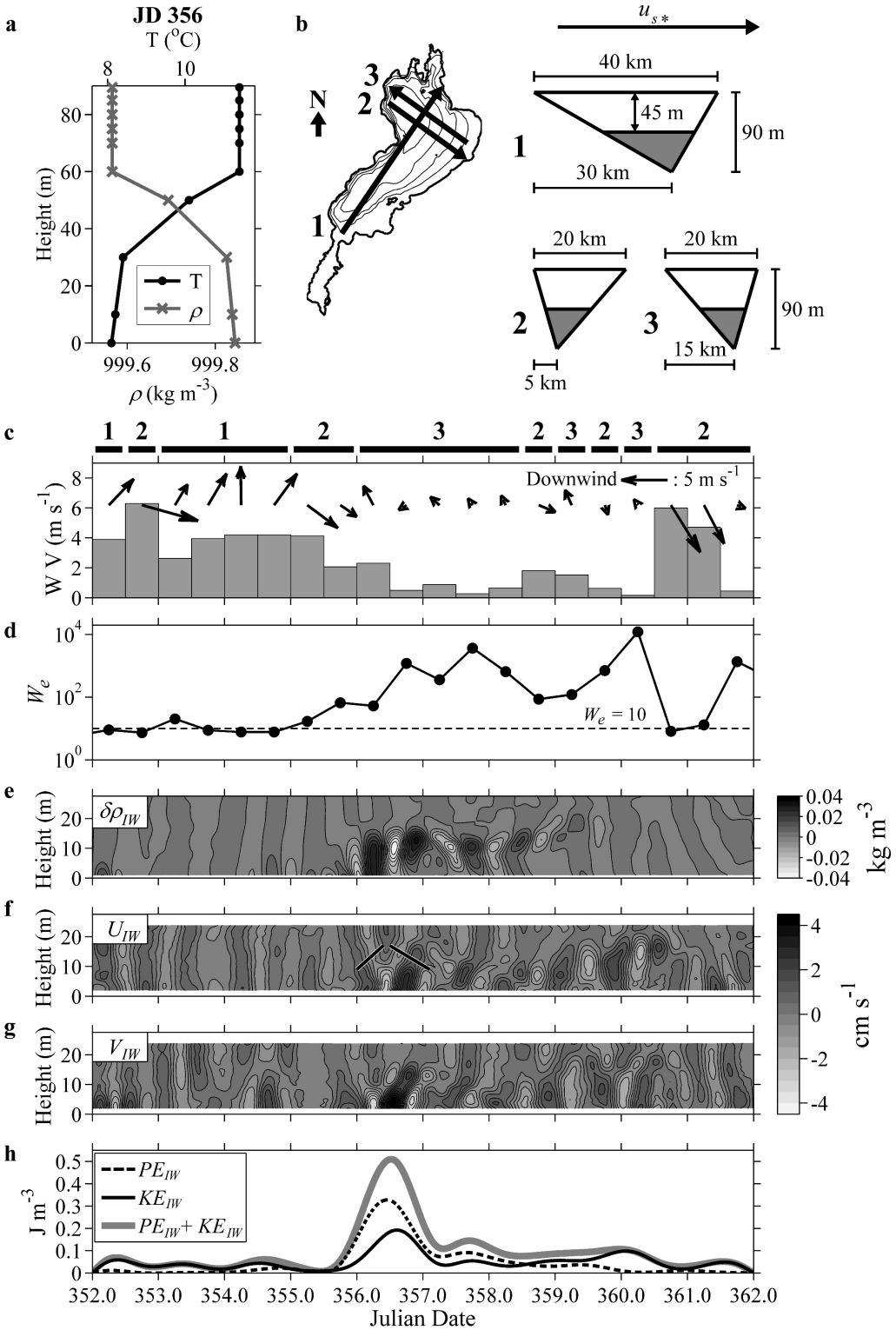

Fig. 2. (a) Vertical profiles observed on JD 356 at station 17B, center of North Basin (Fig. 1a). (b) Approximated wind directions (north upward) and corresponding basin shapes with 2-layer assumption. (c) Half-day averaged wind velocity and wind vectors (north upward). Black bars and numbers at top of panel represent basin shapes in (b), which we used for W_e calculation. (d) Effective Wedderburn number W_e. (e) Density fluctuation due to superinertial internal waves. (f and g) Superinertial internal wave components of eastward and northward velocities. Black lines in (f) indicate estimated propagation directions of internal-wave energy. (h) Depth-averaged internal-wave energy: available potential energy PE_{IW} and kinetic energy KE_{IW}.

restoring force. According to MacIntyre (2008), the thermocline does not tilt when $W_e > 10$. For $W_e < 10$, the thermocline tilts due to wind stress, and the deep water is lifted at the upwind side. When $W_e \sim 1$, the thermocline outcrops to the surface, and for $W_e << 1$ the lake can entirely mix.

To estimate W_e during the observed period, we used a temperature profile at offshore station 17B (Fig. 1a) observed on JD 356 by the environment department of Shiga Prefecture (SPLBED 2010) and assumed a 2-layer stratification with an initial surface layer thickness of 45 m (Fig. 2a and b). The depth-averaged densities of the upper and lower layers were 999.60 and 999.82 kg m^{-3}, respectively. To simplify the calculations, we approximated wind direction and corresponding basin shape into 3 cases (Fig. 2b). We used half-day averaged wind data (Fig. 2c) for the estimation because the wind blowing for half an inertial period is sufficient to establish wind-driven currents, according to the numerical study of Lake Biwa by Oonishi and Imasato (1975).

Modal analysis

We conducted a modal analysis to calculate the periods of basin-scale internal waves assuming a 2-layer stratification. The numerical grid is the same as that used by Shimizu et al. (2007) for Lake Biwa. We used the same upper-layer thickness and layer densities as the Wedderburn number calculation. We included linear bottom friction using the numerical scheme of Shimizu and Imberger (2010). Because detailed data were lacking, we assumed the linear bottom friction coefficient of 1.4×10^{-4} m s^{-1} and the bottom boundary layer thickness to be 10% of the total water depth, for reasons stated later. In the shallower region where the lower layer does not exist, the water column was assumed to be well mixed.

Energetics of internal waves

To detect the arrival and decay of internal waves, we estimated the available potential energy of internal waves PE_{IW} using (Kunze 1993):

$$PE_{IW} = \frac{b^2}{2\bar{N}(z)^2}\rho_0(z), \tag{2}$$

where ρ_0 and $\bar{N}$ are, respectively, the time-averaged density and buoyancy frequency at a depth of z (positive upward); $b = -g\delta\rho_{IW}/\rho_0(z)$ is the buoyancy anomaly; and $\delta\rho_{IW}$ is the density fluctuation due to internal waves. The kinetic energy of internal waves KE_{IW} is given by:

$$KE_{IW} = \frac{1}{2}\left(U_{IW}^2 + V_{IW}^2\right)\rho_0(z), \tag{3}$$

where U_{IW} and V_{IW} are the eastward and northward current velocities induced by internal waves.

In this study, we obtained U_{IW}, V_{IW}, and $\delta\rho_{IW}$ using a band-pass filter with cutoff periods of 10 and 21 h based on the spectral peaks of the observed superinertial internal waves (shown later). Accordingly, the internal-wave energy extracted with this method excluded high-frequency internal waves (e.g., Boegman et al. 2003, Preusse et al. 2010) and subinertial internal waves such as Kelvin waves. We used the same filtering method as Alford et al.

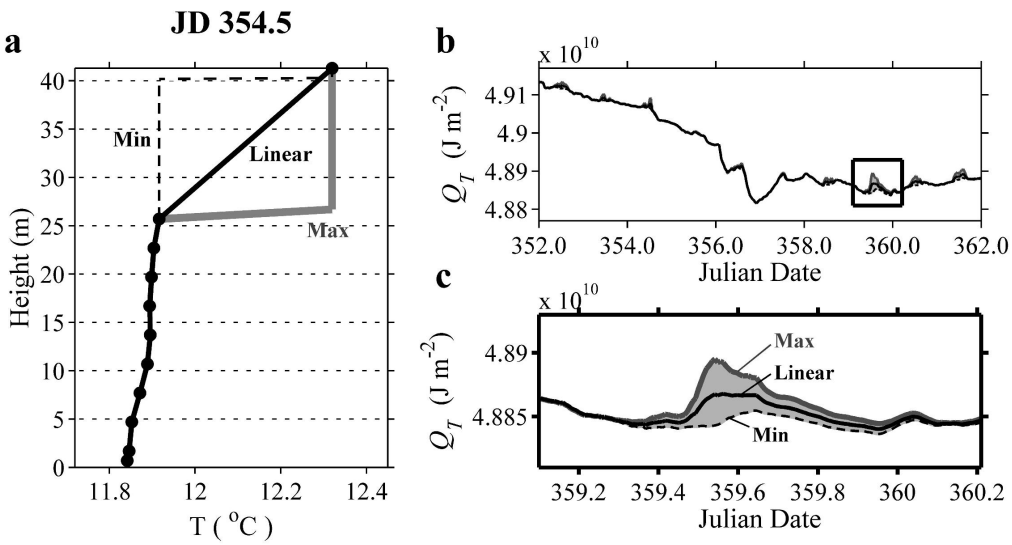

Fig. 3. Comparison of interpolation for surface logger spacing. (a) Example of interpolated temperature profile (observed on JD 354.5). Three cases are compared: linear interpolation (solid black line), minimum estimation of heat content (broken black line), and maximum estimation (gray line). Filled circles on profile denote levels of loggers. (b) Time series of heat content in observed water column. (c) Example of 3 estimated cases from region shown in rectangle indicated in (b).

 DOI: 10.5268/IW-6.3.898

(2012), applying the filter forward and backward to remove phase shift. We then obtained the vertically averaged PE_{IW} and KE_{IW} over a range of 1.9–23.9 m above the bottom, where both the temperature and velocity measurements were available. To emphasize day-scale changes in the energy levels, we used a low-pass filter with a cutoff period of 24 h to smooth PE_{IW} and KE_{IW}.

Heat budget

Heat budget was used to evaluate the contributions of vertical mixing and horizontal advection in observed temperature change. We estimated the heat content Q_T per unit area as:

$$Q_T = C_p \int_{-H}^{0} \rho(z) T(z) dz, \quad (4)$$

where T and ρ are, respectively, the water temperature and density; C_p is the specific heat of fresh water 4.19×10^3 J kg^{-1} K^{-1}; and H is the height of the water column.

The mooring system had large spacing between the surface temperature logger and top of the thermistor chain, ~15 m (Fig. 1b and Table 1). To evaluate the error due to the coarse resolution of the temperature logger in the surface layer, we compared 3 types of interpolation methods for the large spacing (Fig. 3a); the first was a linear interpolation, the second was the minimum estimation of the heat content assuming a 1 m surface layer, and the third was the maximum estimation assuming a uniform surface layer between the surface and top of the thermistor chain. The 3 methods yielded nearly the same results except for brief periods during daytime, largely due to daytime heating at the surface (Fig. 3b and c). The root mean square difference between the maximum and minimum cases was ~8×10^6 J m^{-2}, <8% of the standard deviation of Q_T during the observed period. Because the difference was small, we used the linear interpolation for this study.

We calculated the surface heat flux J_q^0 (positive upward) using the aforementioned meteorological data and observed water temperature. The J_q^0 consists of 4 components (e.g., Clark et al. 1974, Pickard and Emery 1990):

$$J_q^0 = L_w + S_w + H_s + H_l, \quad (5)$$

where L_w is the longwave radiation (Clark et al. 1974) calculated using the longwave emissivity (Dickey et al. 1994); S_w is the absorption of the shortwave radiation affected by the local albedo (Payne 1972); and H_s and H_l are the sensible heat flux and latent heat flux estimated from the empirical models (Fairall et al. 1996), respectively. For simplicity, we ignored the sensible heat flux due to precipitation (Gosnell et al. 1995) because the mean flux due to the observed precipitation was ~1% of the mean J_q^0 during the observed period.

To investigate the heat budget of the water column, we compared the anomaly of local heat content, $Q_T(t_0) - Q_T(t)$, against the time-integrated surface heat flux, $\int_{t_0}^{t} J_q^0 \, dt$, where t_0 = JD 352.0 in this study. The former is equivalent to the total heat exchange of the water column (THEX), and the latter indicates the amount of surface heat exchange (SHEX). Assuming no heat exchange at the bottom boundary, the difference between THEX and SHEX is due to contributions from lateral advection. Note that positive values of SHEX and THEX indicate heat being released from the water column (i.e., cooling of the water column).

Diapycnal mixing

To evaluate mixing due to shear instability, we estimated the 1 m mean gradient Richardson number $Ri = N^2/S^2$, which depends on the stability of stratified shear flows and is the ratio between the buoyancy frequency $N^2 = -(g/\rho_0)\partial\rho/\partial z$ and squared background shear $S^2 = (\partial U/\partial z)^2 + (\partial V/\partial z)^2$, where U and V are the eastward and northward background current velocities, respectively.

We also estimated the turbulent kinetic energy dissipation rate using the observed density profiles. Assuming that the change in stratification is due to diapycnal mixing, the mean dissipation rate from time t_1 to t_2 in the water column between heights H_1 and H_2 is estimated from (MacKinnon and Gregg 2003):

$$\varepsilon_{TOT} = \frac{PE(t_2) - PE(t_1)}{\gamma \rho_0 \Delta t}, \quad (6)$$

where $PE(t) = (H_2 - H_1)^{-1} \int_{H_1}^{H_2} \rho(t,z) g z \, dz$ is the mean potential energy of the water column, $\Delta t = t_2 - t_1$, and γ is the mixing efficiency. We used the parameterization of γ as a function of Ri for $Ri < 1$: $\gamma = 0.005 + 1.7Ri - 1.1Ri^2$ (Lozovatsky and Fernando 2013). For $Ri > 1$, we used the conventional value $\gamma \sim 0.2$ (Osborn 1980). To calculate PE without the contribution of superinertial internal waves, we used the low-pass-filtered time series of density ρ with a cutoff period of 21 h. To assess the cause of the mixing, we compared this total dissipation rate against that due to the following potential mechanisms of diapycnal mixing.

The dissipation rate due to the stress at boundaries was estimated from the conventional law of the wall (Dillon et al. 1981, Dewey and Crawford 1988):

$$\varepsilon_{LOW} = \frac{u_*^3}{kd}, \quad (7)$$

where d is the distance from a boundary, and k is von Karman's constant (~0.41). The friction velocity u_* is u_{s*}

from equation 1 for the surface wind stress but $u_* = C_{Db}^{1/2} U_b$ for the bottom stress, where C_{Db} is the bottom drag coefficient and U_b is the near-bottom current velocity. The bottom drag coefficient was estimated from $C_{Db} = [k/\ln(d/d_0)]^2$, where d_0 is the roughness length (~0.4 mm for unrippled sand bottom; Soulsby 1983). We used the velocity measured at 2.9 m above the bottom for U_b, and the corresponding C_{Db} was ~0.002. We estimated the dissipation due to wind stress ε_{SBL} and that due to bottom stress ε_{BBL}.

The convection due to surface cooling was evaluated using the Monin-Obukhov length scale (Monin and Obukhov 1954):

$$L_{MO} = \frac{u_{s*}^3}{k J_b^0}, \tag{8}$$

where $J_b^0 = (g/\rho)(\alpha J_q^0/C_p)$ is the surface buoyancy flux (positive upward) in which α is the thermal expansion coefficient, and L_{MO} is the distance from the surface in which J_b^0 is equal to ε_{SBL}. Therefore, below this depth, the convective mixing due to J_b^0 dominates the mixing due to wind stress.

Dissipation of the basin-scale internal waves can be caused by bottom friction (e.g., Gloor et al. 2000), Kelvin-Helmholtz instability (e.g., Auger et al. 2013), and wave–wave interactions that cascade energy to high-frequency internal waves (Garrett and Munk 1972, 1975). With the assumptions of no internal-wave energy advection and negligible wave-mean flow interactions, we estimated the dissipation rate of internal-wave energy as:

$$\varepsilon_{IW} = \frac{\Delta PE_{IW} + \Delta KE_{IW}}{\Delta t \, \rho_0}, \tag{9}$$

where $\Delta PE_{IW} = PE_{IW}(t_1) - PE_{IW}(t_2)$ and $\Delta KE_{IW} = KE_{IW}(t_1) - KE_{IW}(t_2)$. Note that because our sampling interval (10 min) was not sufficient to resolve the high-frequency internal waves and because the internal-wave energies PE_{IW} and KE_{IW} were based on the band-pass-filtered time series at 10–21 h, this estimation excludes the contributions of breaking high-frequency internal waves (e.g., Boegman et al. 2003, Preusse et al. 2010) and dissipation of subinertial internal waves.

Results

Background stratification

The vertical temperature profiles at offshore station 17B (Fig. 1a) showed that the stratification started to weaken from September, and the water column became almost uniform by February (Fig. 4). The period of our observations (JD 352–362, 2009) was in the middle of the cooling phase when the lake was weakly stratified.

Atmospheric forcing

During our observations, convective mixing was expected to be active because the surface heat flux was overall positive (cooling), except for brief periods of daytime heating (Fig. 5a). Early in the observation, heat flux during the cooling periods exceeded 400 W m^{-2}, whereas that during the heating periods was around −200 W m^{-2}. From JD 359, heat flux during nighttime cooling had nearly the same magnitude as daytime heating (~200 W m^{-2}).

Moderately strong winds blew steadily until JD 356.0 (Fig. 5b). The northward and southeastward winds were dominant, with wind speeds reaching 5 and 7 m s^{-1}, respectively. Subsequently, the wind speed decreased to ~2 m s^{-1} on JD 356, and the weak wind persisted until JD 360.5 (for 4 d) except for the gusty southeastward wind on JD 358.7. After the period of weak winds, the wind speed increased to >9 m s^{-1} on JD 360.6, and this strong wind lasted for 1 day.

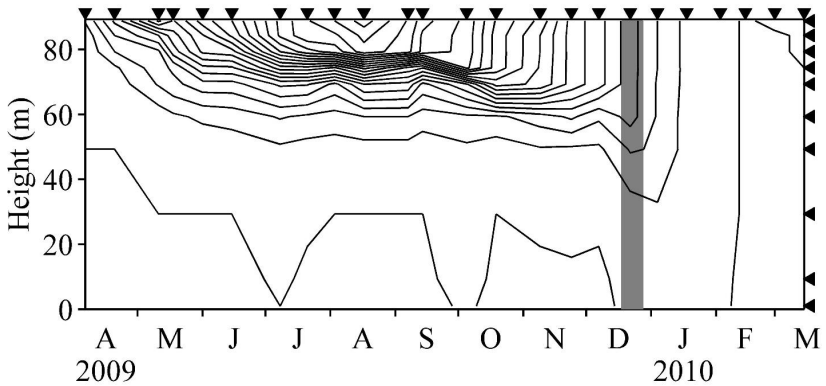

Fig. 4. Vertical thermal structure at center of lake basin (station 17B in Fig. 1a) from April 2009 to March 2010. Data were collected by environment department of Shiga Prefecture (SPLBED 2010). Triangles on top and right axes show date and level of recorded data, respectively. Isotherms were plotted at 1 °C intervals from 8 (bottom) to 28 °C (top). Vertical gray stripe shows our observation period (JD 352.0–362.0).

 DOI: 10.5268/IW-6.3.898

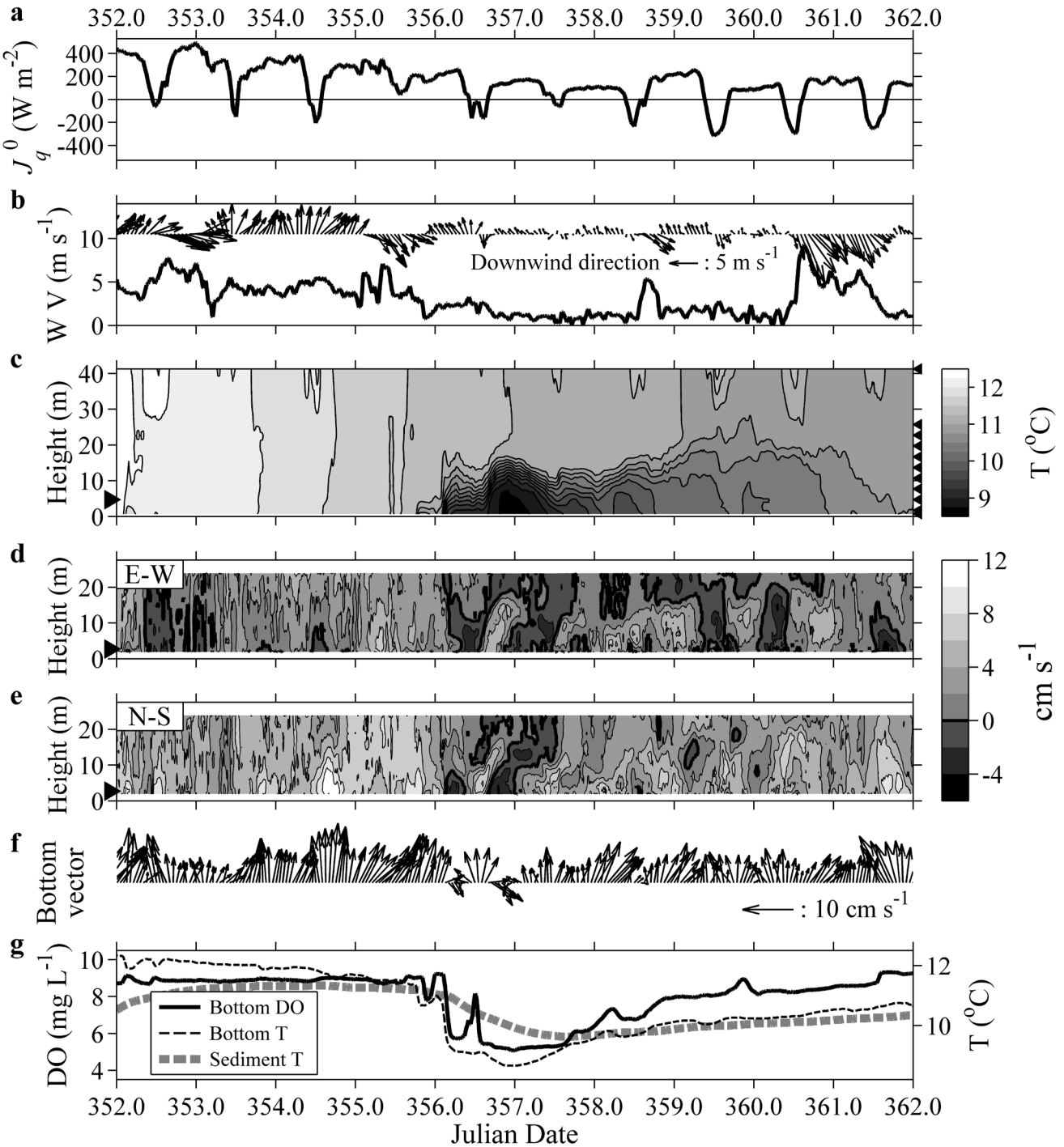

Fig. 5. Time series observed between JD 352.0 and 362.0 at northeastern slope of North Basin. (a) Surface heat flux (positive upward). (b) Wind velocity and wind vector showing downwind direction (north upward). (c) Vertical thermal structure from surface to bottom. Triangles on right axis show levels of temperature loggers. (d and e) Vertical structures of eastward velocity (positive eastward) and northward velocity (positive northward). (f) Current vector (north upward) at bottom layer that corresponds to triangle on left axis of (d) and (e). (g) Oxygen concentration in bottom water (solid black line), bottom water temperature (broken black line), and sediment temperature (broken gray line).

Water temperature and velocity

The water temperature gradually decreased from ~12 to 11.5 °C during JD 352–355 (Fig. 5c). The water column was almost well mixed until JD 355, but a cold water mass appeared near the bottom around JD 356.0 after the period of moderately strong winds (Fig. 5b and c). The minimum temperature of 8.6 °C was observed near the bottom on JD 357.0, whereas the surface water temperature remained >11 °C (Fig. 5c). The cooling of the sediment lagged that of the bottom water, and the sediment was warmer than the bottom water at the beginning of the cold water mass appearance (Fig. 5g). Furthermore, this cold water mass had low DO concentration (explained later). These findings suggest that the cold water mass came from the deep water section because of wind-induced upwelling or baroclinic motions.

Simultaneous with the appearance of the cold water mass, oscillating currents were observed near the bottom (Fig. 5d and e). Between JD 356.0 and 357.5, the near-bottom current vector exhibited clockwise rotation over time (Fig. 5d–f), suggesting the presence of internal waves. The upward/downward phase propagations of U_{IW} and V_{IW} (see JD 356 in Fig. 2f and 5d) imply some downward/upward propagations of internal-wave energy (e.g., Alford et al. 2012). The rotary spectra of the near-bottom currents over JD 352.0–362.0 exhibit peaks in the clockwise component around the periods of 19 and 12 h (Fig. 6b), which are shorter than the inertial period (T_f = 20.7 h at 35°20′N). The power spectral density of the bottom water temperature computed from the detrended time series also shows peaks around the periods of 19 and 12 h (Fig. 6a), consistent with those found in the velocity data. The thicknesses of the oscillating currents and cold water were almost the same, ~20 m (Fig. 5c–e); thus, the movement of the cold water mass was associated with the clockwise rotating currents with superinertial frequencies.

After its appearance, the cold water mass gradually became thicker and warmer with slight fluctuations (Fig. 5c and g). The water column eventually became almost uniform on JD 362.0 (Fig. 5c).

Dissolved oxygen concentration

The near-bottom DO concentration rapidly decreased from 9 to 5 mg L^{-1} on JD 356 (Fig. 5g), coinciding with a sudden drop in the bottom water temperature (Fig. 5g). Low DO concentration indicates that the water originated from the deeper part of the lake, which was hypoxic in December 2009 (Jiao et al. 2011). The rapid decreases in oxygen concentration on JD 356.1 and 356.5 were accompanied by the southeastward currents (Fig. 5f and g) toward the shallower side of the slope (Fig. 1a); therefore, the cold low-oxygen water intrusion with rotating currents suggests that the deeper water was lifted up the slope by basin-scale baroclinic motions. DO concentration gradually recovered and reached the same level as that before the intrusion event on JD 362.0 (Fig. 5g).

Discussion

Wedderburn number

At the beginning of the cold water intrusion around JD 356.0 (Fig. 5), winds were weak (~2 m s^{-1} in a half-day average; Fig. 2c) and the estimated W_e was ~10^2 (Fig. 2d). Afterward, wind speed remained <2 m s^{-1} until JD 360.5

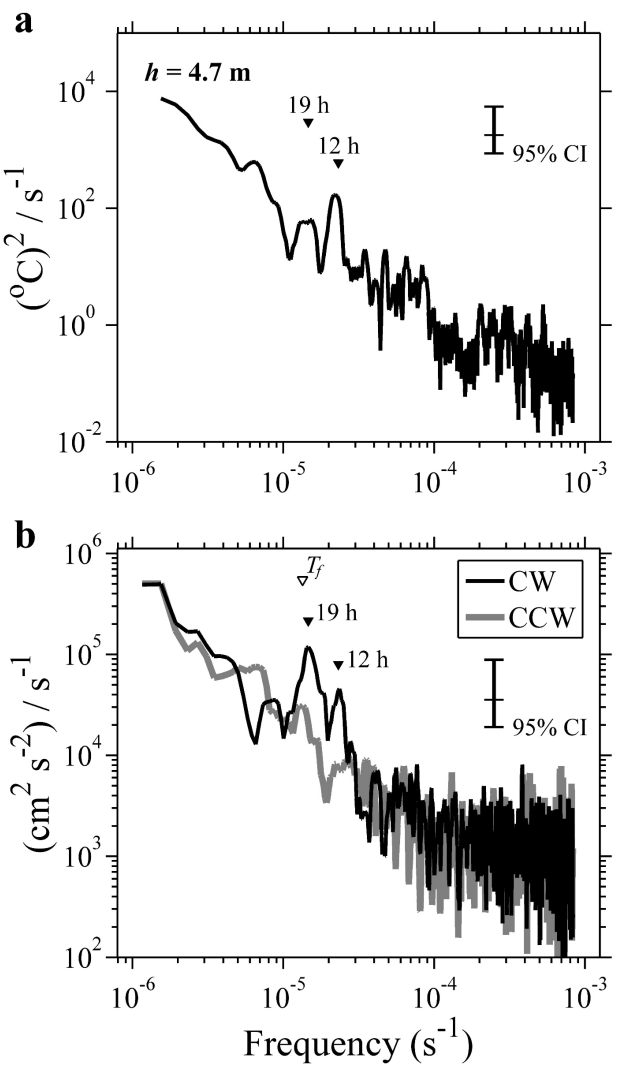

Fig. 6. (a) Power spectral density of bottom water temperature (4.7 m from bottom, indicated by triangle on left axis of Fig. 5c). (b) Rotary spectra of bottom current (shown in Fig. 5f). CW = clockwise (black); CCW = counterclockwise (gray). Bar at upper right in each panel represents 95% confidence interval.

 DOI: 10.5268/IW-6.3.898

and W_e ranged from 10^2 to 10^4. Wind-induced upwelling was thus unlikely to occur during the period in which the cold water mass occupied the bottom layer. Moderately strong winds (≥4 m s^{-1}), however, blew toward the northeast and southeast prior to the intrusion event, and W_e was mostly <10 until JD 355.0 (Fig. 2c and d). Because the water column was almost uniform until JD 355.0 (Fig. 5c), a deepening of the thermocline could have occurred at the observation site, a finding consistent with previous studies on this lake. Okamoto (1969) observed thermocline deepening at the northern shore during northward winds, and Endoh et al. (1981) reported thermocline deepening at the eastern shore during southeastward winds. Subsequently, as the wind abated, basin-scale baroclinic motions such as Kelvin waves could have propagated, and the thermocline was locally lifted up to the observation site. The change in wind direction from northeastward to southeastward (JD 354.5–355.5; Fig. 2c) increased W_e to >10 (Fig. 2d) because northeastward winds (from gentle slope direction; Fig. 1a) are more efficient than southeastward winds (from steep slope direction) in tilting the thermocline in this lake (Shintani et al. 2010).

In addition to the large-scale tilting of the thermocline, the observed clockwise rotating currents with superinertial frequencies (Fig. 5f and 6b) suggest the presence of Poincaré waves. According to Valipour et al. (2015b), near-inertial internal Poincaré waves are excited by short impulsive wind events with a duration of 0.25–0.5T_f, and clockwise rotating winds are also effective in inducing the Poincaré waves. At the end of the period of long-lasting winds (JD 353–355; Fig. 5b), we observed impulsive wind events lasting ~5 h (~0.25T_f, JD 355.1 and 355.4) and clockwise rotating winds that shifted from northward to southeastward (JD 354.5–355.5). Based on the results of Valipour et al. (2015b), these wind events might contribute to the excitation of the internal Poincaré waves. Because our results suggest the presence of both basin-scale Kelvin and Poincaré waves, the observed cold water mass intrusion was likely attributed to a combination of these waves.

Basin-scale internal waves

We conducted a modal analysis to investigate the relationship between wind-driven basin-scale Kelvin and Poincaré waves and superinertial oscillatory currents and the observed cold water intrusion, which required a bottom boundary layer thickness (Shimizu and Imberger 2010). Unfortunately, the 3 m vertical interval of thermistors was too coarse to accurately determine bottom boundary layer thickness, and to the best of our knowledge, detailed measurements of the bottom boundary layer in Lake Biwa are unavailable. Hence, we estimated the bottom boundary layer thickness as follows. Visual inspection (Fig. 5c–e) during the cold water intrusion suggested that the bottom boundary layer thickness at site Y (~40 m depth) was in the range of 2–5 m. We used the following equation to estimate the bottom boundary layer thickness h_b (Valipour et al. 2015a):

$$h_b = \frac{1.8u_*}{f\left(1+\frac{N^2}{f^2}\right)^{1/4}}. \quad (10)$$

We used the mean bottom friction velocity ($u_* \sim 2.5 \times 10^{-3}$ m s^{-1}) and mean buoyancy frequency in the thermocline ($N^2 \sim 7.5 \times 10^{-5}$ s^{-2}) at the site (~40 m depth). Using these numbers, we obtained $h_b \sim 5$ m. Because the bottom boundary layer thickness typically increases with water depth (Lemckert et al. 2004, Marti and Imberger 2006), we assumed the bottom boundary layer thickness to be 10% of the total water depth.

The modal analysis yielded horizontal mode 1 Kelvin and Poincaré waves with periods of 132 and 17.0 h, respectively. There were 7 Poincaré wave modes (17.0, 15.8, 15.0, 13.7, 13.0, 12.6, and 12.3 h periods) between the inertial and semidiurnal periods. The period of the mode 1 Kelvin wave suggests that the lag between strong wind until JD 355 and cold water intrusion around JD 357 (Fig. 5b and c) was due to the propagation of the Kelvin wave crest after the relaxation of the wind forcing. Although the modes of Poincaré waves in the rotary spectra from the 10 d time series (Fig. 6b) cannot be distinguished, the observed clockwise rotation of currents with superinertial frequencies is consistent with the characteristics of Poincaré waves.

To provide some support that the cold water intrusion and superinertial clockwise currents were due to a combination of basin-scale Kelvin and Poincaré waves, we also computed the evolution of basin-scale internal wave modes under wind forcing following Shimizu and Imberger (2008, 2010). Because the modal analysis lacks advection and mixing, it is not an ideal tool for analyzing the observed phenomena; however, it is still useful to check the consistency (or a lack of it) with the observations. We included all the internal gravity wave modes with periods between 11 and 132 h (34 modes), including the aforementioned Kelvin and Poincaré waves. The wind field was constructed as in Shimizu et al. (2007) from 5 land-based meteorological stations of the Japan Meteorological Agency. We started the simulation from the rest on JD 333. Because site Y was located at ~40 m depth, shallower than the quiescent thermocline depth, we inspected the output at a location ~2.2 km west-northwest of site Y, where water depth was ~55 m.

The results reproduced the timing (but not the amplitude) of the slow thermocline uplift due to the arrival of the horizontal mode 1 Kelvin wave (Fig. 7a). The horizontal mode 1–7 Poincaré waves, excited during the wind events before JD 355.0, contributed to the uplift by adding superinertial fluctuations. Poincaré waves also induced a peak-to-peak current amplitude of ~0.04 m s^{-1} in the lower layer with semidiurnal to inertial periods (Fig. 7b). The velocity amplitude is consistent with the superinertial components of the observed currents U_{IW} and V_{IW} in the cold water mass (Fig. 2f and g). Although these currents were induced ~2 km from the observation site, the cold water intrusion could have been induced by a combination of basin-scale Kelvin and Poincaré waves.

The timing of the superinertial wave excitation (before JD 355.0; Fig. 7a) is inconsistent with that of the impulsive winds and rotating winds around JD 355.0 (Fig. 5b), suggested as the trigger of the Poincaré waves in the previous section. Although the excitation mechanism is still unclear, both the results from the modal analysis and Valipour et al. (2015b) suggest that the observed winds were able to provoke internal Poincaré waves.

Energetics of superinertial internal waves

The time series of PE_{IW} and KE_{IW} reveal the arrival and decay of the superinertial internal waves. Subsequent to the wind disturbance and relaxation, the internal-wave energy rapidly increased on JD 356 (Fig. 2c–h). At the end of the intrusion, the depth-averaged energy dropped around JD 357 but was still higher than that before the intrusion (Fig. 2h). Subsequently, PE_{IW} decreased gradually while KE_{IW} slightly increased between JD 358 and 360. This KE_{IW} gain could be due to the stronger wind around JD 359.0 (Fig. 2c).

After the KE_{IW} enhancement, KE_{IW} eventually decreased to the base level on JD 362.0 (Fig. 2h). The superinertial internal waves persisted over 5 d after the cold water intrusion. As shown later, the decay of internal-wave energy was primarily due to bottom friction.

Heat budget

The gradual increase in thickness of the intruded cold water and slow recovery of near-bottom DO concentration (Fig. 5c and g) suggest that significant diapycnal mixing was taking place. We used heat budget estimates to separate the contributions of lateral advection and diapycnal mixing in the observed temperature change. Because the sediment did not contribute to the formation of the cold water (Fig. 5g), we assumed zero heat flux at the bottom; therefore, the difference between THEX and SHEX can be attributed to the lateral heat exchange due to advection.

The THEX exhibits greater increase than SHEX during the cold water mass intrusion (Fig. 8a). Until JD 354.5, THEX was almost equivalent to SHEX, indicating that the lateral advection had little effect on heat exchange. From JD 354.5, THEX increased more rapidly than SHEX. In particular, the cold water mass intrusion (JD 356.0–357.5) provided a dramatic gain in THEX. Although THEX decreased at the end of the intrusion, the increase in THEX from JD 356.0 to JD 357.5 was ~7.8×10^7 J m^{-2}, greater than the SHEX increase of ~1.5×10^7 J m^{-2} during the same period.

By contrast, after the intrusion, THEX and SHEX increased at almost the same rate from JD 357.5 to 362.0 (Fig. 8a); thus, the heat transport due to advection was negligible during this period. The disappearance of the cold water mass and the recovery of oxygen concentration (Fig. 5c and g) are considered due to diapycnal mixing.

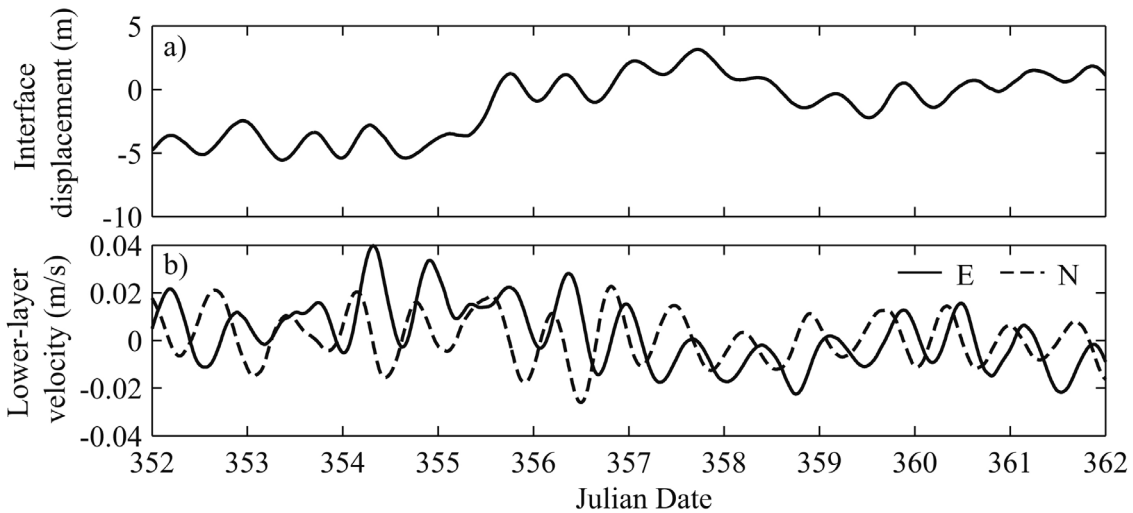

Fig. 7. (a) Interface displacement at ~2.2 km west-northwest of site Y calculated using modal analysis. (b) Eastward (solid line) and northward (broken line) velocities in lower layer at same location.

 DOI: 10.5268/IW-6.3.898

Overall, the cold water intrusion and subsequent diapycnal mixing provided a net cooling of 5.1×10^7 J m^{-2} to the water column during JD 356.0–362.0. The corresponding average heat flux was ~98 W m^{-2}, 1.4 times greater than the average surface heat flux (71 W m^{-2}) over the same period.

Diapycnal mixing

To determine possible causes of the diapycnal mixing, we first considered the shear-induced mixing using the observed N^2 and S^2. The buoyancy frequency N^2 decreased from $>10^{-3.8}$ to $<10^{-5.0}$ s^{-2} during JD 357.5–362.0, and S^2 often increased to $>10^{-4.2}$ s^{-2} between the cold water and overlying water (Fig. 8b and c). Because the water was not stratified except for this interface, 1 m mean *Ri* was estimated when $N^2 \geq 10^{-5}$ s^{-2} (Fig. 8d). At the interfacial layer, *Ri* occasionally dropped below 1 but was mostly >0.25, that is the critical value of the necessary condition for Kelvin-Helmholtz instability and subsequent turbulent mixing. The mean *Ri* during JD 357.5–362.0 was 6.2, which excludes the highest and lowest 1% of the *Ri* data values. The 95% confidence interval was 5.9–6.6, assuming that mean *Ri* follows a normal distribution. Because the instability with $Ri < 0.25$ is often detected at fine spatial and temporal scales (~0.1 m and ~N s^{-1}; e.g., Boegman et al. 2003), however, our mooring systems did not resolve such small-scale unstable layers. Hence, local small-scale mixing could have occurred.

In addition to shear-induced turbulence, diapycnal mixing can be supported by the physical processes at boundaries. We calculated ε_{TOT} (equation 6) as the total turbulent kinetic energy dissipation rate required for observed potential energy increase and compared it with the dissipation rates estimated for possible physical processes (Table 2). The dissipation rates were averaged from t_1 = JD 357.5 to t_2 = JD 362.0 (after the intrusion) and the height between H_1 = 1.9 m and H_2 = 23.9 m, where both the temperature and velocity were measured. Because the mean *Ri* between t_1 and t_2 was 6.2, we used the mixing efficiency $\gamma = 0.2$ for equation 6. The total averaged dissipation rate was $\varepsilon_{TOT} = 2.0 \times 10^{-8}$ W kg^{-1}. In the case of $Ri = 0.25$, γ is 0.36 according to Lozovatsky and Fernando (2013). The corresponding ε_{TOT} is roughly 50% smaller than that with $\gamma = 0.2$; however, the dissipation rates are of the same order. Thus, we used $\varepsilon_{TOT} = 2.0 \times 10^{-8}$ W kg^{-1} for our analysis.

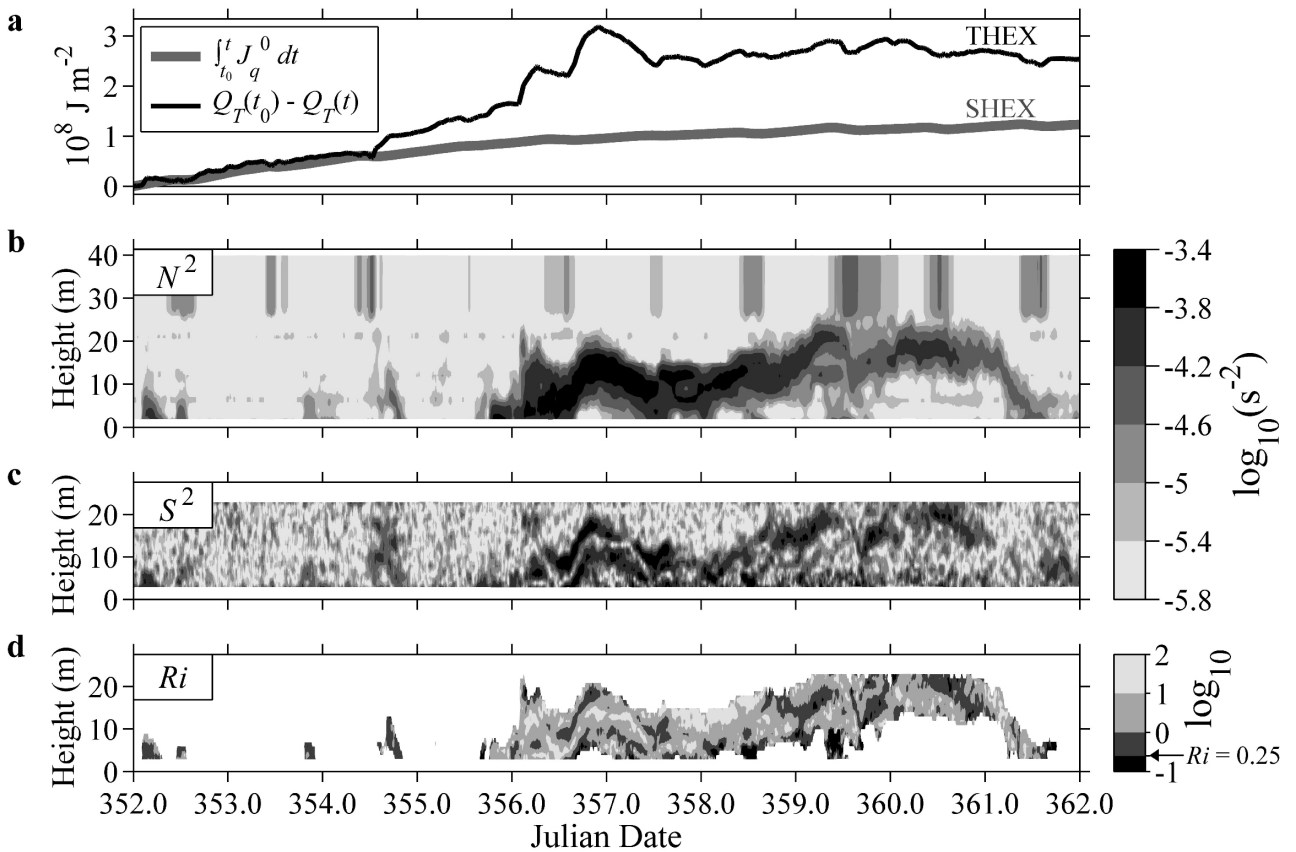

Fig. 8. (a) Surface heat exchange (SHEX, thick gray line, positive upward) and total heat exchange of observed water column (THEX, thin black line). (b) Squared buoyancy frequency. (c) Squared velocity shear. (d) Gradient Richardson number estimated for $N^2 \geq 10^{-5}$ s^{-2}.

Table 2. Estimates of turbulent kinetic energy dissipation rate and buoyancy flux averaged over JD 357.5–362.0 and 1.9–23.9 m height. SupIW = superinertial internal waves; SubIW = subinertial internal waves. * is not depth-averaged but is value at surface.

Symbol	Property/Cause of mixing	Estimate (W kg^{-1})
ε_{TOT}	Total dissipation	2.0×10^{-8}
ε_{IW}	Decay of SupIW energy	3.3×10^{-10}
ε_{SBL}	Surface wind stress	9.3×10^{-9}
ε_{BBL}	Bottom stress	4.5×10^{-9}
ε^{L}_{BBL}	ε_{BBL} without SupIW velocity	3.1×10^{-9}
ε^{H}_{BBL}	ε_{BBL} without SubIW velocity	1.8×10^{-10}
J_b^0	Surface cooling	(1.3×10^{-8})*

The dissipation rate of the superinertial internal waves was evaluated from the decay of the band-pass-filtered energy (equation 9). The estimated average dissipation rate ε_{IW} was 3.3×10^{-10} W kg^{-1}, nearly the noise level of turbulent microstructure measurement (Lueck et al. 2002); therefore, dissipation of the superinertial internal waves was unlikely to cause the observed diapycnal mixing.

Wind stress provided $\varepsilon_{SBL} = 9.3 \times 10^{-9}$ W kg^{-1}, and bottom stress led to $\varepsilon_{BBL} = 4.5 \times 10^{-9}$ W kg^{-1}. Because both dissipation rates are in the same order, both wind and bottom stress were likely to be major contributors to the diapycnal mixing. We also estimated the dissipation rate due to the bottom stress calculated from the velocity without the superinertial internal wave components ε^{L}_{BBL}. We used low-pass-filtered velocity time series with a cutoff period of 21 h to remove the superinertial internal wave components. The estimated ε^{L}_{BBL} was 3.1×10^{-9} W kg^{-1}, ~70% of ε_{BBL}. The remaining 30% of ε_{BBL} should be caused by enhancement of bottom currents due to the superinertial internal waves. In addition, we estimated the dissipation rate from high-pass-filtered near-bottom current velocity excluding the subinertial internal wave components ε^{H}_{BBL} with a cutoff period of 21 h. The estimated ε^{H}_{BBL} of 1.8×10^{-10} W kg^{-1} was of the same order as ε_{IW}, suggesting that bottom stress was a major sink of the superinertial internal-wave energy. Note that ε_{BBL} of 4.5×10^{-9} W kg^{-1} was greater than $\varepsilon^{L}_{BBL} + \varepsilon^{H}_{BBL} = 3.3 \times 10^{-9}$ W kg^{-1} because ε at an arbitrary depth in the boundary layer (equation 7) is proportional to U^3. The remaining $\varepsilon_{BBL} - (\varepsilon^{L}_{BBL} + \varepsilon^{H}_{BBL}) = 1.2 \times 10^{-9}$ W kg^{-1} could dissipate due to cross terms of subinertial and superinertial flows.

The average surface buoyancy flux J_b^0 was 1.3×10^{-8} W kg^{-1}, roughly the same level as ε_{SBL}. During nighttime with weak winds (around JD 358.0, 359.0, and 360.0; Fig. 5a and b), L_{MO} was mostly <1 m, indicating that thermal convection dominated the wind-induced mixing in the upper mixed layer and likely reached the bottom cold water. Therefore, convection due to surface cooling is another major contributor to the diapycnal mixing.

In summary, the diapycnal mixing after the cold water intrusion was not induced by a single process but was probably driven by a combination of multiple processes. In particular, surface wind stress, convection due to the surface cooling, and bottom stress due to the currents were roughly equally important to the mixing of intruded cold water. It is estimated that the bottom stress-induced mixing was enhanced by the superinertial internal waves by 30%.

Acknowledgements

This work was supported by the Global Environmental Research Fund (Fa-084) of the Ministry of the Environment, Japan, and was also supported by a Grant-in-Aid for Scientific Research (20244079) from the Japan Society for the Promotion of Science. We express our gratitude to Dr. Michio Kumagai at Ritsumeikan University for his constructive advice as well as his help in surveys throughout this study. We thank Mr. Junichi Kawamura and the staff of LBERI as well as the captain and crew of R/V Hakken-go for their support in the survey. We are grateful to Professor Naoko Hasegawa at Ochanomizu University, Professor Daisuke Kitazawa, and Mr. Masamitsu Kajinami at the University of Tokyo for their help as well as their scientific and technical advice about mooring observations. We thank Ms. Lynn Allmon for her editorial advice during the preparation of the manuscript. We gratefully acknowledge Dr. Ilia Ostrovsky at Israel Oceanographic & Limnological Research Institute for his helpful comments on this study.

References

Akitomo K, Tanaka K, Kumagai M, Jiao C. 2009a. Annual cycle of circulations in Lake Biwa, part 1: model validation. Limnology. 10:105–118.

Akitomo K, Tanaka K, Kumagai M. 2009b. Annual cycle of circulations in Lake Biwa, part 2: mechanisms. Limnology. 10:119–129.

Alford MH, Cronin MF, Klymak JM. 2012. Annual cycle and depth penetration of wind-generated near-inertial internal waves at Ocean

 DOI: 10.5268/IW-6.3.898

Station Papa in the Northeast Pacific. J Phys Oceanogr. 42:889–909.

Auger G, Yamazaki H, Nagai T, Jiao C, Kumagai M. 2013. Hypolimnetic turbulence generation associated with superposition of large-scale internal waves in a strongly stratified lake: Lake Biwa, Japan. Limnology. 14:229–238.

Boegman L. 2009. Currents in stratified water bodies 2: internal waves. In: Likens GE, editor. Encyclopedia of inland waters, Vol. 1. Oxford (UK): Elsevier. p. 539–558.

Boegman L, Imberger J, Ivey GN, Antenucci JP. 2003. High-frequency internal waves in large stratified lakes. Limnol Oceanogr. 48:895–919.

Clark NE, Eber L, Laurs RM, Renner JA, Saur JFT. 1974. Heat exchange between ocean and atmosphere in the eastern North Pacific for 1961–71. NOAA Technical Reports NMFS SSRF-682.

Dewey RK, Crawford WR. 1988. Bottom stress estimates from vertical dissipation rate profiles on the continental shelf. J Phys Oceanogr. 18:1167–1177.

Dickey TD, Manov DV, Weller RA, Siegel DA. 1994. Determination of longwave heat flux at the air-sea interface using measurements from buoy platforms. J Atmos Ocean Tech. 11:1057–1078.

Dillon TM, Richman JG, Hansen CG, Pearson MD. 1981. Near-surface turbulence measurements in a lake. Nature. 290:390–392.

Endoh S, Okamoto I, Nakai M. 1981. Circular currents in the North Basin of Lake Biwa (I) seasonal variation of circular currents deduced from water temperature distributions. Jpn J Limnol. 42:144–153. Japanese.

Fairall CW, Bradley EF, Rogers DP, Edson JB, Young GS. 1996. Bulk parameterization of air-sea fluxes for Tropical Ocean-Global Atmosphere Coupled-Ocean Atmosphere Response Experiment. J Geophys Res. 101(C2):3747–3764.

Fer I, Lemmin U, Thorpe SA. 2001. Cascading of water down the sloping sides of a deep lake in winter. Geophys Res Lett. 28:2093–2096.

Garrett C, Munk W. 1972. Space-time scales of internal waves. Geophys Fluid Dyn. 3:225–264.

Garrett C, Munk W. 1975. Space-time scales of internal waves: a progress report. J Geophys Res. 80:291–297.

Gloor M, Wüest A, Imboden DM. 2000. Dynamics of mixed bottom boundary layers and its implications for diapycnal transport in a stratified, natural water basin. J Geophys Res. 105(C4):8629–8646.

Gosnell R, Fairall CW, Webster PJ. 1995. The sensible heat of rainfall in the tropical ocean. J Geophys Res. 100(C9):18437–18442.

[JMA] Japan Meteorological Agency. 2002. Kako no kisho deta daunrodo [Download of previous meteorological data] [cited 10 May 2014]. Available from: http://www.data.jma.go.jp/gmd/risk/obsdl/index.php. Japanese.

Jiao C, Aoki S, Okumura Y, Minami M, Yada M, Ishikawa K, Nakajima T, Ishikawa T, Tsujimura S. 2011. Biwako no teisansoka no jittaihaaku oyobi hokkoseitaikei ni ataeru eikyo no haaku ni kansuru kaiseki monitaringu [Analytic monitoring to understand the actual conditions of hypoxia and its influence on the ecosystem in the North Basin of Lake Biwa]. Shigaken Biwako Kankyo Kagaku Kenkyu Senta Kenkyu Hokokusyo [Research Report of Lake Biwa Environmental Research Institute]. 7:150–181. Japanese.

Kawanabe H, Nishino M, Maehata M, editors. 2012. Lake Biwa: interactions between nature and people. New York (NY): Springer.

Kumagai M, Ishikawa K, Ishiguro N. 2003. Impacts of global warming on large lakes. In: Franks S, Blöschl G, Kumagai M, Musiake K, Rosbjerg D, editors. Water resources systems—water availability and global change. Oxford (UK): IAHS Press. p. 65–69.

Kunze E. 1993. Submesoscale dynamics near a seamount. Part II: the partition of energy between internal waves and geostrophy. J Phys Oceanogr. 23:2589–2601.

Lemckert C, Antenucci J, Saggio A, Imberger J. 2004. Physical properties of turbulent benthic boundary layers generated by internal waves. J Hydraul Eng. 130:58–69.

Lozovatsky ID, Fernando HJS. 2013. Mixing efficiency in natural flows. Philos T R Soc A. 371:20120213, doi:10.1098/rsta.2012.0213

Lueck RG, Wolk F, Yamazaki H. 2002. Oceanic velocity microstructure measurements in the 20th century. J Oceanogr. 58:153–174.

MacIntyre S. 2008. Describing fluxes within lakes using temperature arrays and surface meteorology. Verh Internat Verein Limnol. 30:339–344.

MacKinnon JA, Gregg MC. 2003. Mixing on the late-summer New England shelf—solibores, shear, and stratification. J Phys Oceanogr. 33:1476–1492.

Marshall J, Schott F. 1999. Open-ocean convection: observations, theory, and models. Rev Geophys. 37:1–64.

Marti CL, Imberger J. 2006. Dynamics of the benthic boundary layer in a strongly forced stratified lake. Hydrobiologia. 568:217–233.

Melack JM, Jellison R. 1998. Limnological conditions in Mono Lake: contrasting monomixis and meromixis in the 1990s. Hydrobiologia. 384:21–39.

Monin AS, Obukhov AM. 1954. Basic laws of turbulent mixing in the surface layer of the atmosphere. Tr Akad Nauk SSSR Geophiz Inst. 24:163–187.

Monismith SG. 1985. Wind-forced motions in stratified lakes and their effect on mixed-layer shear. Limnol Oceanogr. 30:771–783.

Nagai T, Yamazaki H, Nagashima H, Kantha LH. 2005. Field and numerical study of entrainment laws for surface mixed layer. Deep-sea Res Part II. 52:1109–1132.

Okamoto I. 1969. Time variation of water temperature in Lake Biwa-ko (V): wind effects on the distribution of water temperature. Memoirs of Faculty of Education, Shiga University Natural Science. 19:81–91. Japanese.

Oonishi Y, Imasato N. 1975. Study on the currents in Lake Biwa (II) – barotropic responses to the uniform wind of a finite duration. J Oceanogr Soc Jpn. 31:53–60.

Osborn TR. 1980. Estimates of the local rate of vertical diffusion from dissipation measurements. J Phys Oceanogr. 10:83–89.

Payne RE. 1972. Albedo of the sea surface. J Atmos Sci. 29:959–970.

Peeters F, Kipfer R. 2009. Currents in stratified water bodies 1: density-driven flows. In: Likens GE, editor. Encyclopedia of inland waters, Vol. 1. Oxford (UK): Elsevier. p. 530–538.

Pickard GL, Emery WJ. 1990. Descriptive physical oceanography: an introduction. 5th enlarged ed. Oxford (UK): Pergamon Press.

Preusse M, Peeters F, Lorke A. 2010. Internal waves and the generation of turbulence in the thermocline of a large lake. Limnol Oceanogr. 55:2353–2365.

Rueda FJ, Schladow SG, Pálmarsson SÓ. 2003. Basin-scale internal wave dynamics during a winter cooling period in a large lake. J Geophys Res. 108(C3):3097, doi:10.1029/2001JC000942

[SPLBED] Shiga Prefecture Lake Biwa Environment Department. 2010. Shiga no kankyo 2010—Shiryo hen [White paper on environment, Shiga 2010—database]. Otsu (JP). Japanese.

Shimizu K, Imberger J. 2008. Energetics and damping of basin-scale internal waves in a strongly stratified lake. Limnol Oceanogr. 53:1574–1588.

Shimizu K, Imberger J. 2010. Seasonal differences in the evolution of damped basin-scale internal waves in a shallow stratified lake. Limnol Oceanogr. 55:1449–1462.

Shimizu K, Imberger J, Kumagai M. 2007. Horizontal structure and excitation of primary motions in a strongly stratified lake. Limnol Oceanogr. 52:2641–2655.

Shintani T, de la Fuente A, Niño Y, Imberger J. 2010. Generalizations of the Wedderburn number: parameterizing upwelling in stratified lakes. Limnol Oceanogr. 55:1377–1389.

Soulsby RL. 1983. The bottom boundary layer of shelf seas. In: Johns B, editor. Physical oceanography of coastal and shelf seas. Amsterdam (NL): Elsevier. p. 189–266.

Valipour R, Bouffard D, Boegman L. 2015a. Parameterization of bottom mixed layer and logarithmic layer heights in central Lake Erie. J Great Lakes Res. 41:707–718.

Valipour R, Bouffard D, Boegman L, Rao YR. 2015b. Near-inertial waves in Lake Erie. Limnol Oceanogr. 60:1522–1535.

Yoshimizu C, Yoshiyama K, Tayasu I, Koitabashi T, Nagata T. 2010. Vulnerability of a large monomictic lake (Lake Biwa) to warm winter event. Limnology. 11:233–239.

 DOI: 10.5268/IW-6.3.898